Supporting Information

Frozen Slab Method Mediated Sulfur-Affinitive Single-Atom Catalysts for Efficient Reversible Sodium Storage

Kai Cui[†, a], *Zijia Qi*[†, b], *Dominik Legut*[c, d], *Wanxiang Zhao*[e], *Biao Chen*[b], *Ningning Wu*[*, f, g], *Qiuyu Zhang*[*, a], *Tianshuai Wang*[*, a, h]

[a] School of Chemistry and Chemical Engineering, Northwestern Polytechnical University, Xi'an, 710129, P.R. China.

[b] School of Materials Science and Engineering, Tianjin University, Tianjin, 300350, P. R. China.

[c] IT4Innovations, VSB-Technical University of Ostrava, 17. listopadu 2172/15, 708 00 Ostrava, Czech Republic.

[d] Department of Condensed Matter Physics, Faculty of Mathematics and Physics, Charles University, Ke Karlovu 3, 121 16 Prague 2, Czech Republic.

[e] Suzhou Nuclear Power Research Institute, Suzhou 215004, China.

[f] School of Materials Science & Engineering and State Key Laboratory of Reliability and Intelligence of Electrical Equipment, P.R. China.

[g] School of Electrical Engineering, Hebei University of Technology, Tianjin 300401, P. R. China.

[h] Chongqing Science and Technology Innovation Center of Northwestern Polytechnical University, Chongqing 401135, P. R. China.

E-mail: wuningning69@139.com (N. Wu); qyzhang@nwpu.edu.cn (Q. Zhang); tianshuai@nwpu.edu.cn (T. Wang).

† Kai. Cui and Zijia Qi contributed equally to this work

Table of Contents

Figure S17. The (a) charge transfer and (b) binding energy between C-SAV, C-SAFe, C-SANi and MoS_2.

Figure S18. (a) GDC profiles of MoS_2/C-SAV. (b) Rate performance of MoS_2/C-SAV, MoS_2/C-SAFe, and MoS_2/C-SANi.

Figure S19. (a) GITT profiles of MoS_2/C-SAV, MoS_2/C-SAFe, and MoS_2/C-SANi. (b) Voltage *vs*. time profiles for a single GITT of MoS_2/C-SAV during the discharging process. Na^+ diffusion coefficients of MoS_2/C-SAV, MoS_2/C-SAFe, and MoS_2/C-SANi in the (c) discharging and (d) charging processes.

Table S1. The d band center of the metal atoms and the p band center of the N atoms in the C-SAMs substrate and in the frozen slab after S-atom adsorption on C-SAMs.

Table S2. The adsorption energies (E_{ads}, eV) of Na, S and Na_2S on C-SAMs.

Table S3. The frozen slab adsorption energies (E_{fro}, eV) of Na, S and Na_2S on C-SAMs.

Table S4. The Integrated Crystal orbital Hamilton population (ICOHP) values of the M-S bonds when C-SAMs adsorbs S.

Table S5. The ICOHP values of the Na-S bonds in Na_2S when C-SAMs adsorbs Na_2S.

Table S6. The features used in the SISSO computation.

Table S7. Mathematical operators employed in SISSO calculation.

Table S8. SISSO descriptor formula and its corresponding coefficients.

Table S9. Prediction errors of $E_{bar}(Na_2S)$ using SISSO descriptor.

Table S10. Comparison of rate performance of MoS_2/C-SAV with MoS_2-based anode materials for SIBs reported previously.

Table S11. Comparison of long-life cycling performance of MoS_2/C-SAV with MoS_2-based anode materials for SIBs reported previously.

References

Supplementary Methods

DFT calculations. The projector augmented wave (PAW) formalism of density functional theory as implemented in the Vienna Ab-initio Simulation Package (VASP) was used in the system energy and electronic structure calculations[1]. The Gaussian smearing method was used and the width of smearing was chosen as 0.05 eV and the energy cutoff for plane-wave expansion of the PAWs was set to 500 eV. To decouple the periodic replicas, a vacuum layer of approximately 15 Å in thickness was inserted in the vertical direction. The DFT-D3 functional was applied to consider the effect of the physical van der Waals interaction in all calculated simulations[2]. To model the catalyst surface, the Brillouin zone was sampled using Monkhorst-Pack scheme with a k-point mesh of 2×2×1[3]. The structure relaxation was continued until the forces and energies on all the atoms were converged to less than 0.01 eV/Å and 1×10^{-5} eV. The decomposition barrier for Na_2S was determined by climbing image-nudged elastic band[4].

SISSO calculations. The text utilizes version 3.3 of SISSO for multi-task regression. The code used is sourced from the website https://github.com/rouyang2017/SISSO. The input files for SISSO computation can be found in the folder "input templates" within the compressed package. SISSO has been employed to predict the surface adsorption energies of various materials, including single-metal atoms, metallic alloys, and metallic oxides, demonstrating excellent performance in high-dimensional spaces[5]. The data used for training is sourced from the DFT database. In this work, we have selected 11 physical quantities as features (listed in Table S6) based on the open-source database. Subsequently, we iterated the process within the defined dimension: "Feature space construction → Selection of the subspace through Independent Selection (SIS) → Identification of descriptors through Sparse Operator (SO)", thereby obtaining the SISSO descriptors.

Materials Synthesis.

Synthesis of C-SAM. C-SAV was synthesized via the modified salt template method[6]. 8.5 g of NaCl, 0.6 g of glucose, 1.2 g of dicyandiamide, and 19.6 mg of vanadyl sulfate were dissolved in 100 mL of deionized water. The resulting solution was transferred to a spray dryer to remove water, yielding a three-dimensional porous C-SAV gel precursor. This precursor was then annealed in a tube furnace at 750 °C for 2 h under an Ar atmosphere, with a heating rate of 3 °C/min and cooling to 400 °C at a rate of 5 °C/min. The resulting product was washed three times with deionized water to remove NaCl and subsequently dried in a vacuum oven at 60 °C to obtain C-SAV. By replacing 19.6 mg of vanadyl sulfate with 58.6 mg of ammonium ferric citrate or 29.9 mg of nickel acetate tetrahydrate, C-SAFe and C-SANi were obtained, respectively.

Synthesis of MoS_2/C-SAM. MoS_2/PC-SAV was prepared via the solvothermal method. 45 mg of C-SAV and 90 mg of ammonium thiomolybdate were dispersed in a mixed solvent of 15 mL deionized water and 15 mL ethanol under ultrasonication for 2 h. The suspension was then transferred to a 50 mL Teflon-lined stainless-steel autoclave and heated at 190 °C for 24 h. The black product was collected by centrifugation and washed with deionized water and ethanol. Subsequently, the product was calcined at 600 °C for 2 h under a 5% H_2/Ar atmosphere to enhance the crystallinity of MoS_2. For comparison, MoS_2/C-SAFe and MoS_2/C-SANi were synthesized under identical solvothermal conditions by replacing C-SAV with C-SAFe and C-SANi, respectively.

Materials characterization. The morphological and structural characteristics were examined using SEM (Hitachi S4800) and TEM (JEOL JEM-2100F). AC-STEM-ADF images were performed at 60 kV (FEI TitanThemis G2). XRD patterns were acquired by Bruker D8 Advance. Raman spectra were performed by Renishaw in-Via Raman Microscope RE04. XPS was collected in Thermo K-Alpha+. XAS measurements were collected at XAFCA@SSLS.

Electrochemical Measurements. Electrodes were fabricated by mixing the active materials (MoS_2/C-SAV, MoS_2/C-SAFe, and MoS_2/C-SANi) with Super P carbon (as conductive additive) and sodium carboxymethyl cellulose (as binder) in a weight ratio of 7:1.5:1.5. The prepared slurry was coated on Cu foil and dried at 80 ° C for 24 hours. The mass load of the electrode is around 1.2 mg cm^{-1}. CR2032 coin-type half-cells were assembled in an Ar-filled glove box, using sodium metal as the counter electrode, a borosilicate glass microfiber filter as the separator, and $NaPF_6$ (1M) in Diglyme as the electrolyte. The GDC profiles were performed using the NEWARE Battery Test System (MIHW.200-160CH-B, Shenzhen, China).

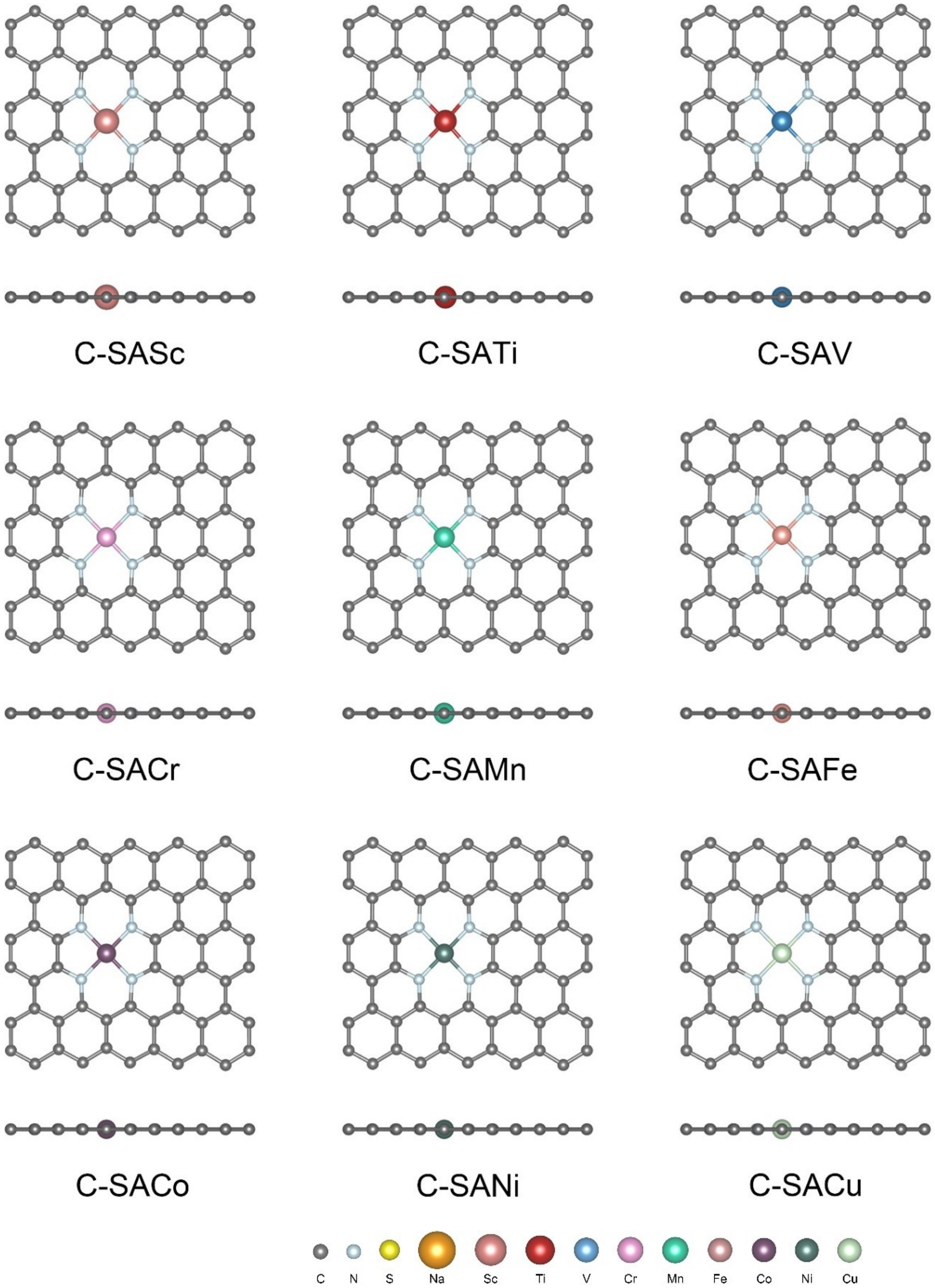
C-SASc

C-SATi

C-SAV

C-SACr

C-SAMn

C-SAFe

C-SACo

C-SANi

C-SACu

Figure S1. The optimized C-SAMs (M = Sc, Ti, V, Cr, Mn, Fe, Co, Ni, Cu) configurations.

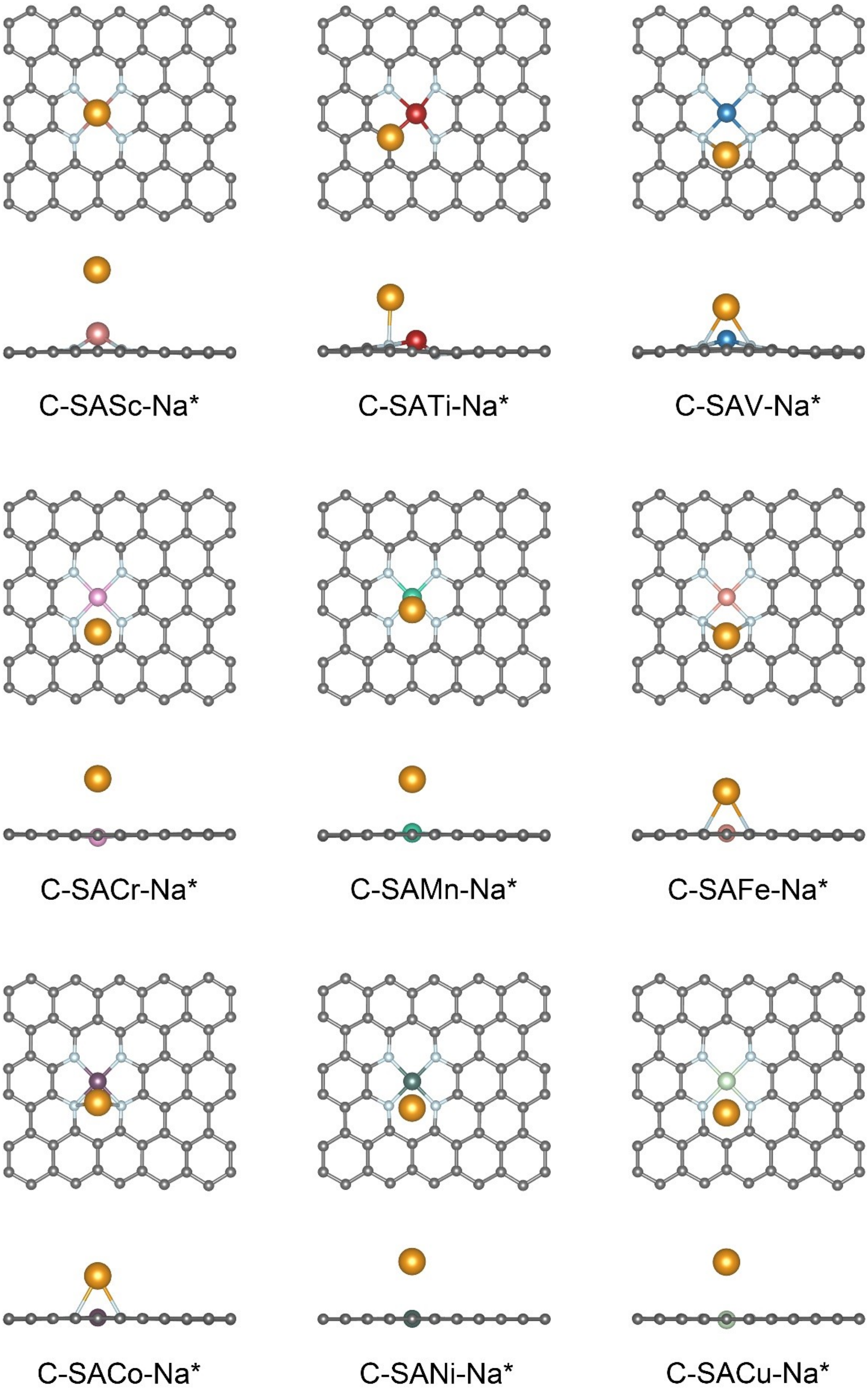

C-SASc-Na* C-SATi-Na* C-SAV-Na*

C-SACr-Na* C-SAMn-Na* C-SAFe-Na*

C-SACo-Na* C-SANi-Na* C-SACu-Na*

Figure S2. The optimized structures of C-SAMs adsorbing Na.

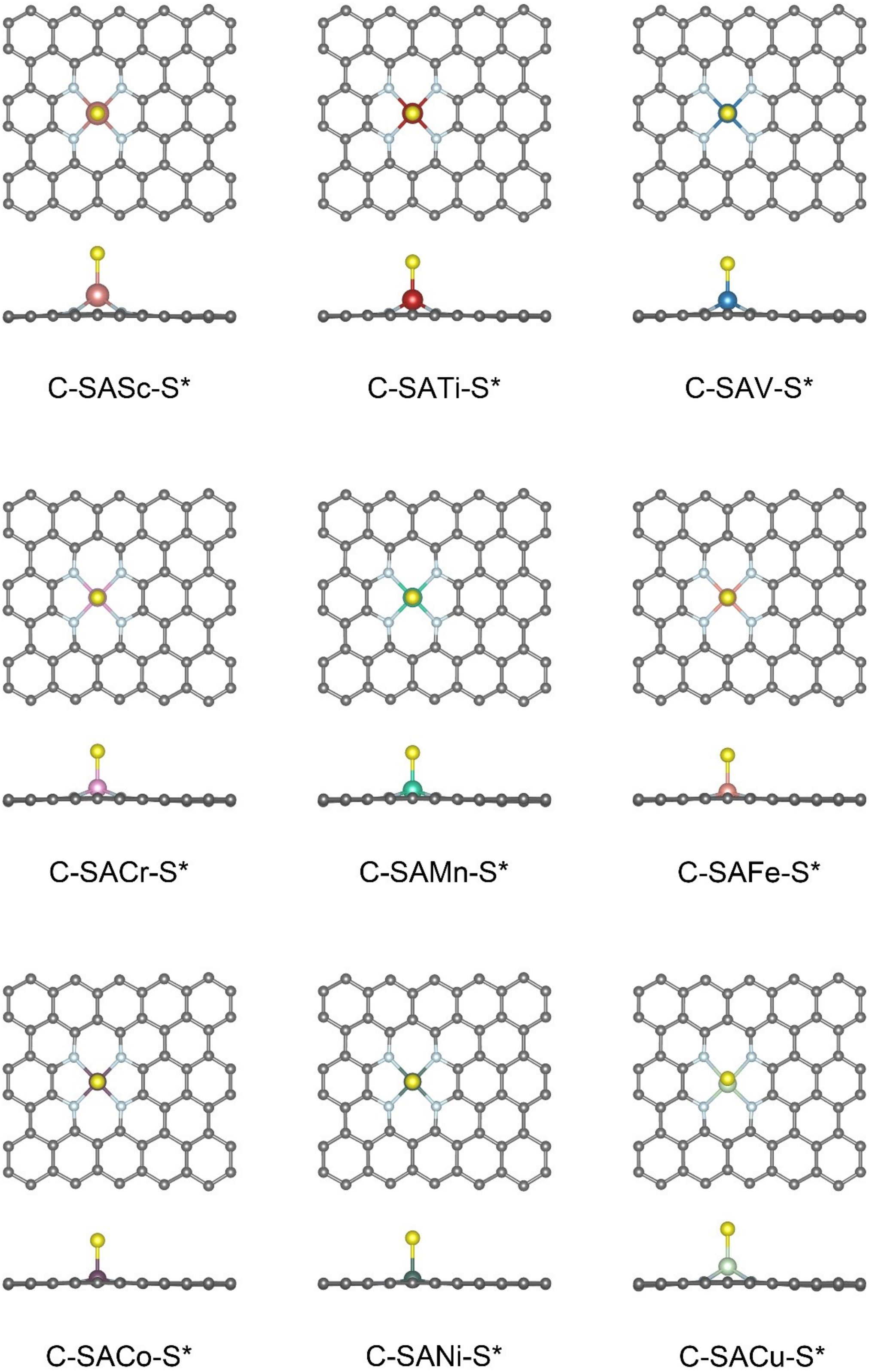

C-SASc-S* C-SATi-S* C-SAV-S*

C-SACr-S* C-SAMn-S* C-SAFe-S*

C-SACo-S* C-SANi-S* C-SACu-S*

Figure S3. The optimized structures of C-SAMs adsorbing S.

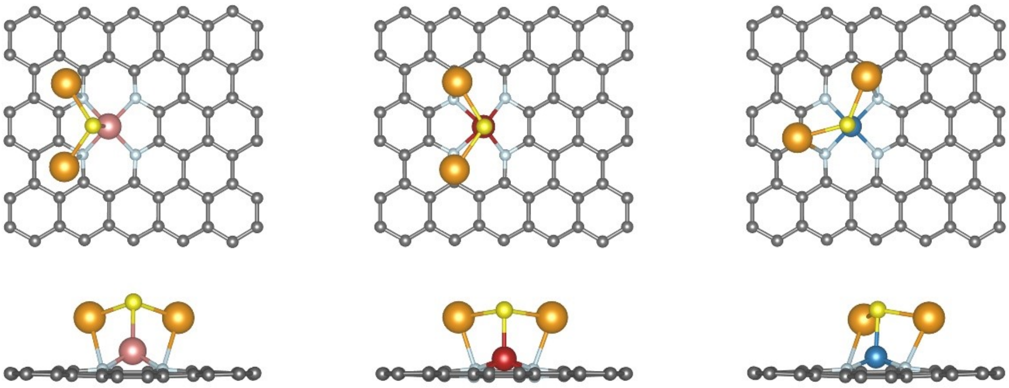

C-SASc-Na_2S* C-SATi-Na_2S* C-SAV-Na_2S*

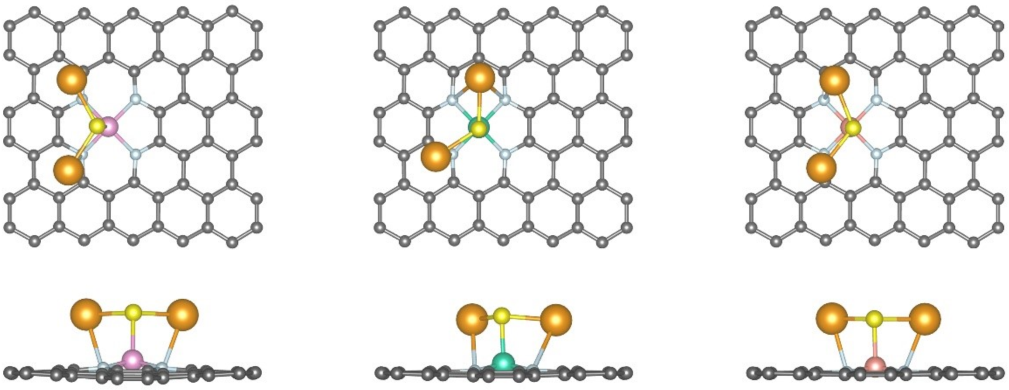

C-SACr-Na_2S* C-SAMn-Na_2S* C-SAFe-Na_2S*

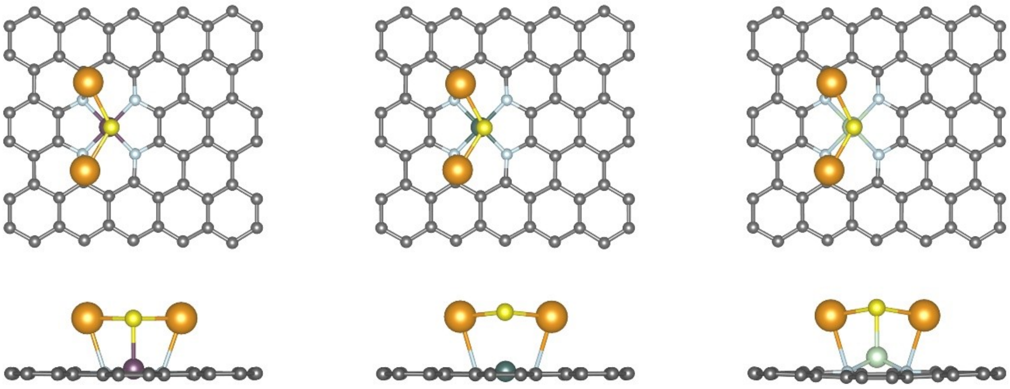

C-SACo-Na_2S* C-SANi-Na_2S* C-SACu-Na_2S*

Figure S4. The optimized structures of C-SAMs adsorbing Na_2S.

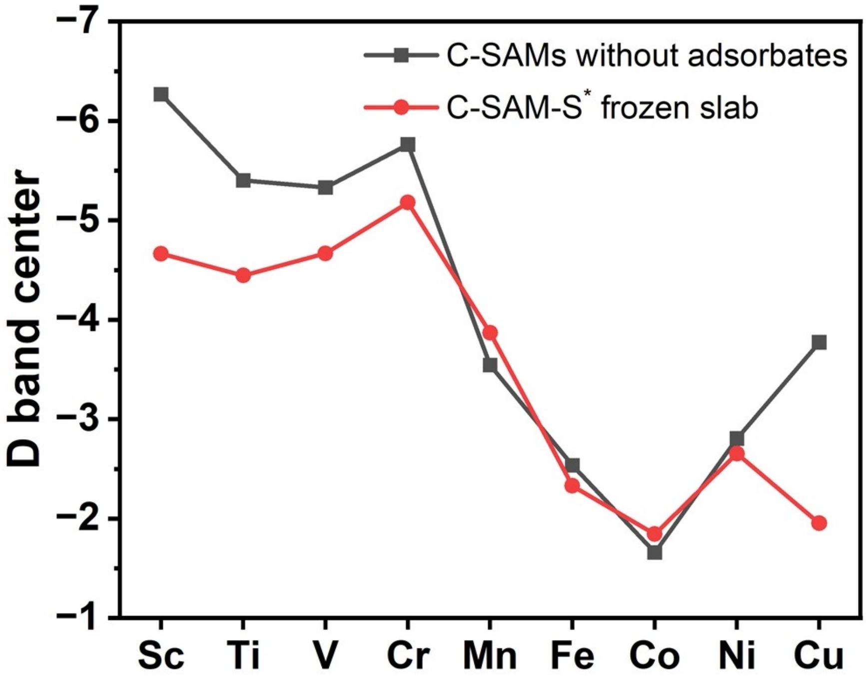

Figure S5. The d band center of the metal atoms in the C-SAMs substrate and in the frozen slab after S adsorption on C-SAMs.

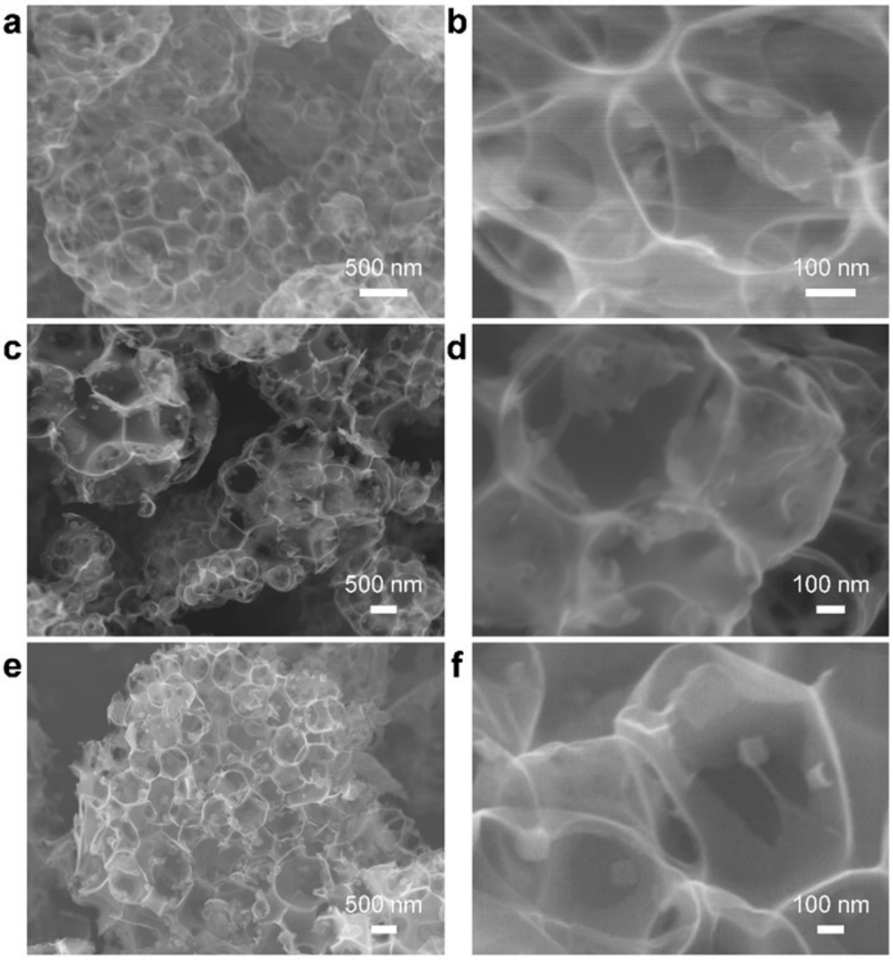

Figure S6. SEM images of (a, b) C-SAV, (c, d) C-SAFe, and (e, f) C-SANi.

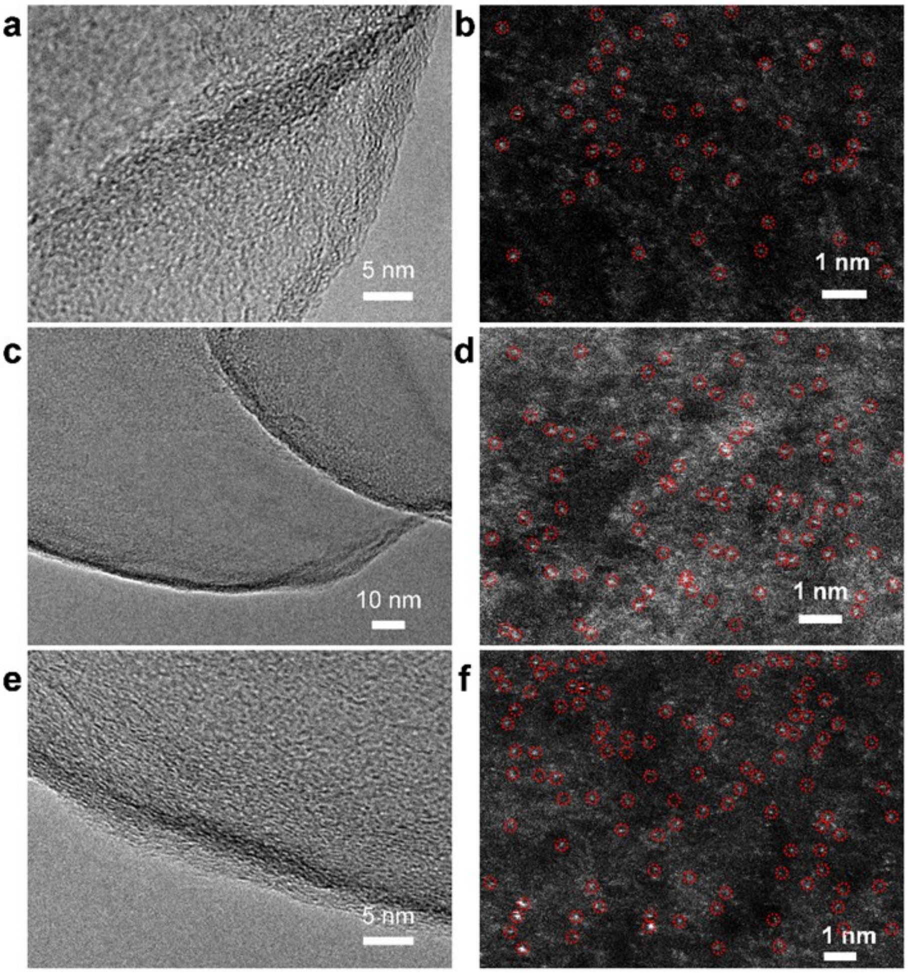

Figure S7. TEM images of (a) C-SAV, (c) C-SAFe, and (e) C-SANi. AC-TEM images of (b) C-SAV, (d) C-SAFe, and (f) C-SANi.

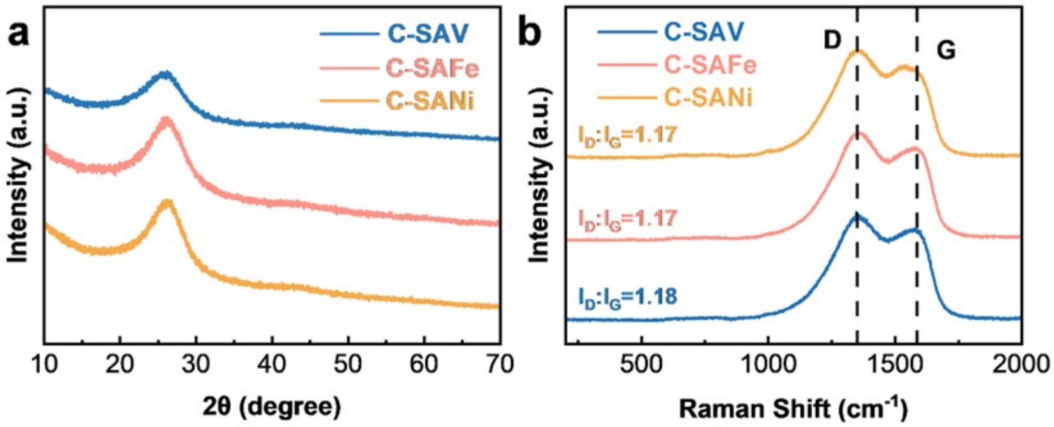

Figure S8. (a) XRD and (b) Raman of C-SAV, C-SAFe, and C-SANi.

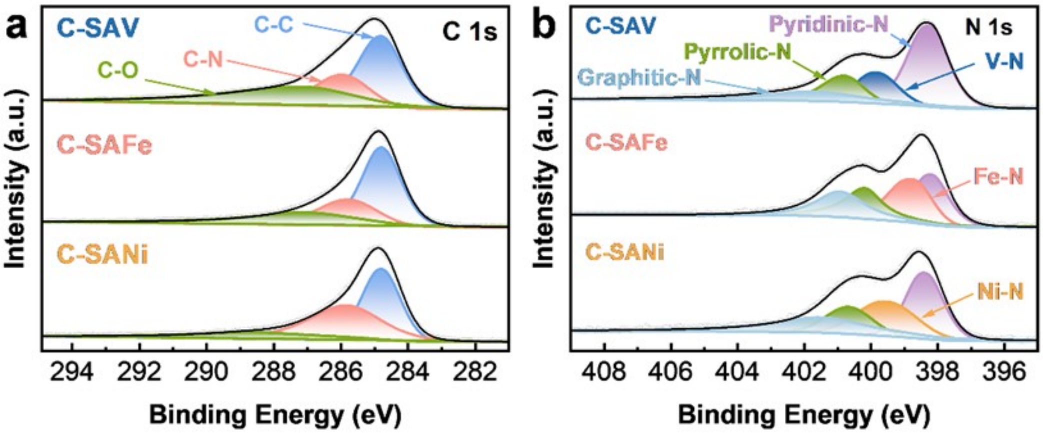

Figure S9. High-resolution XPS spectra of (a) C and (b) N for C-SAV, C-SAFe, and C-SANi.

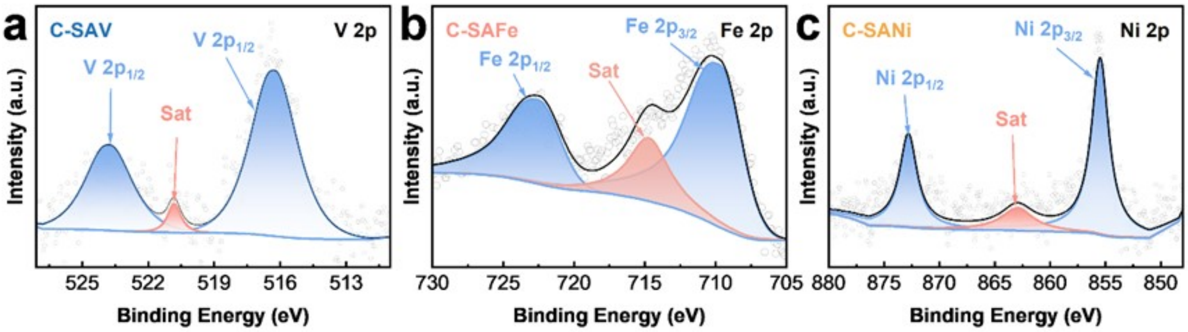

Figure S10. High-resolution XPS spectra of (a) V for C-SAV, (b) Fe for C-SAFe, and (c) Ni for C-SANi.

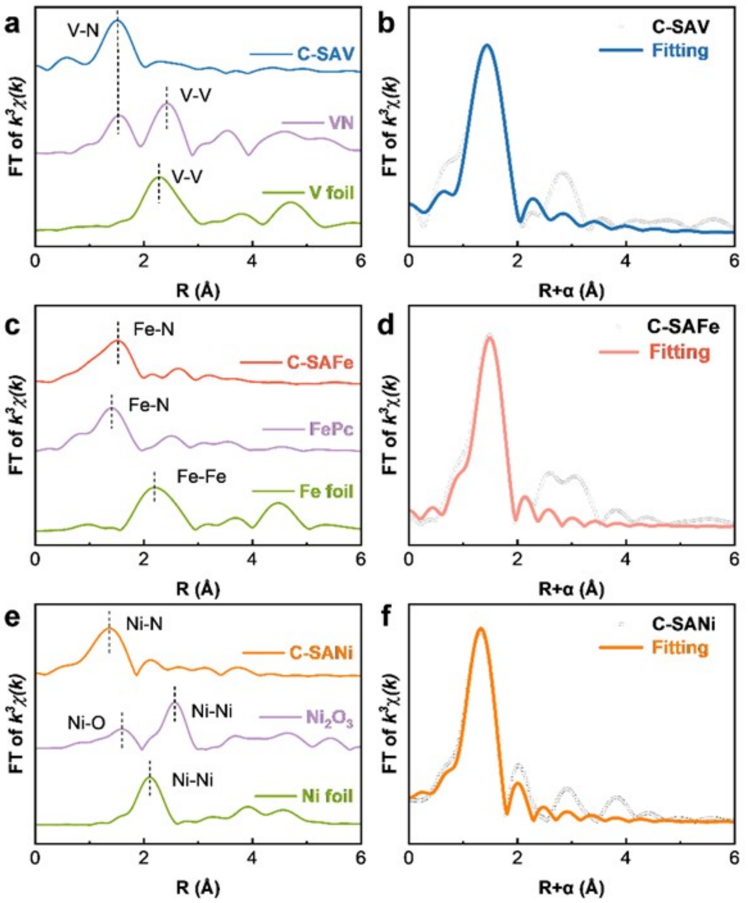

Figure S11. FT-EXAFS of (a) C-SAV, (c) C-SAFe, and (e) C-SANi. EXAFS fitting of (b) C-SAV, (d) C-SAFe, and (f) C-SANi.

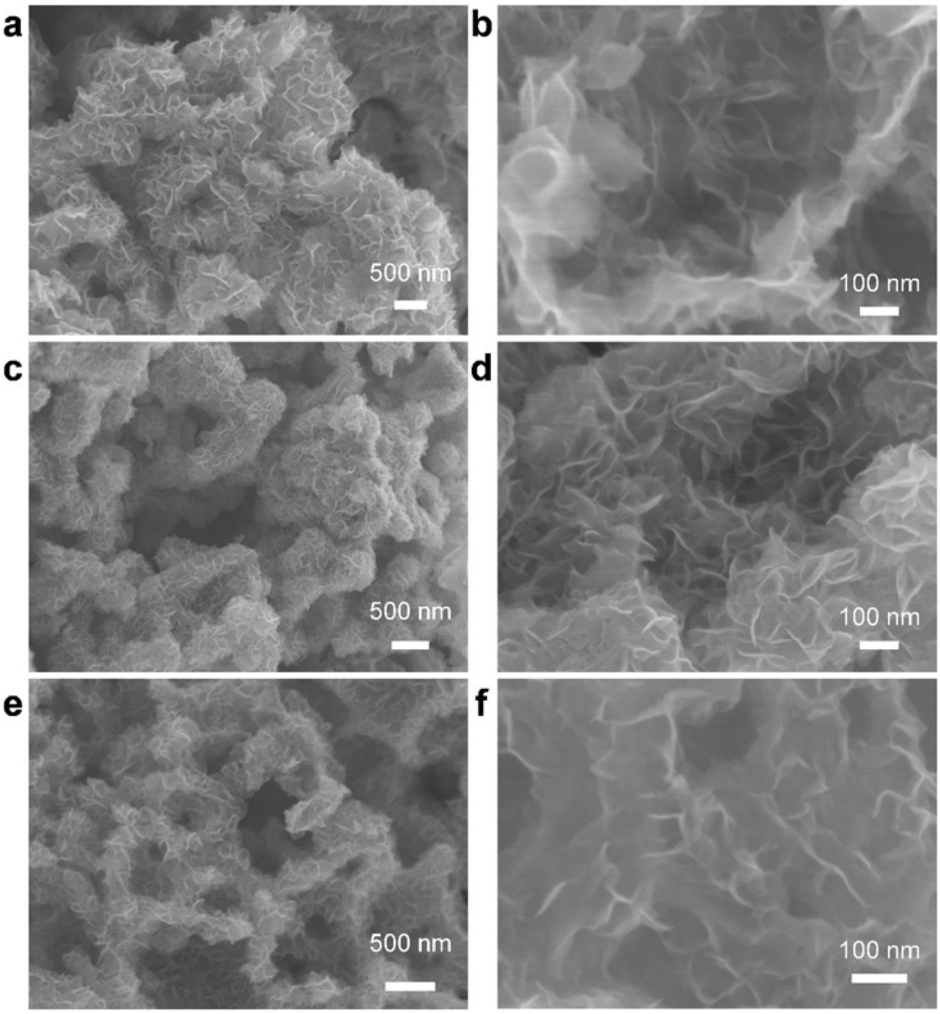

Figure S12. SEM images of (a, b) MoS_2/C-SAV, (c, d) MoS_2/C-SAFe, and (e, f) MoS_2/C-SANi.

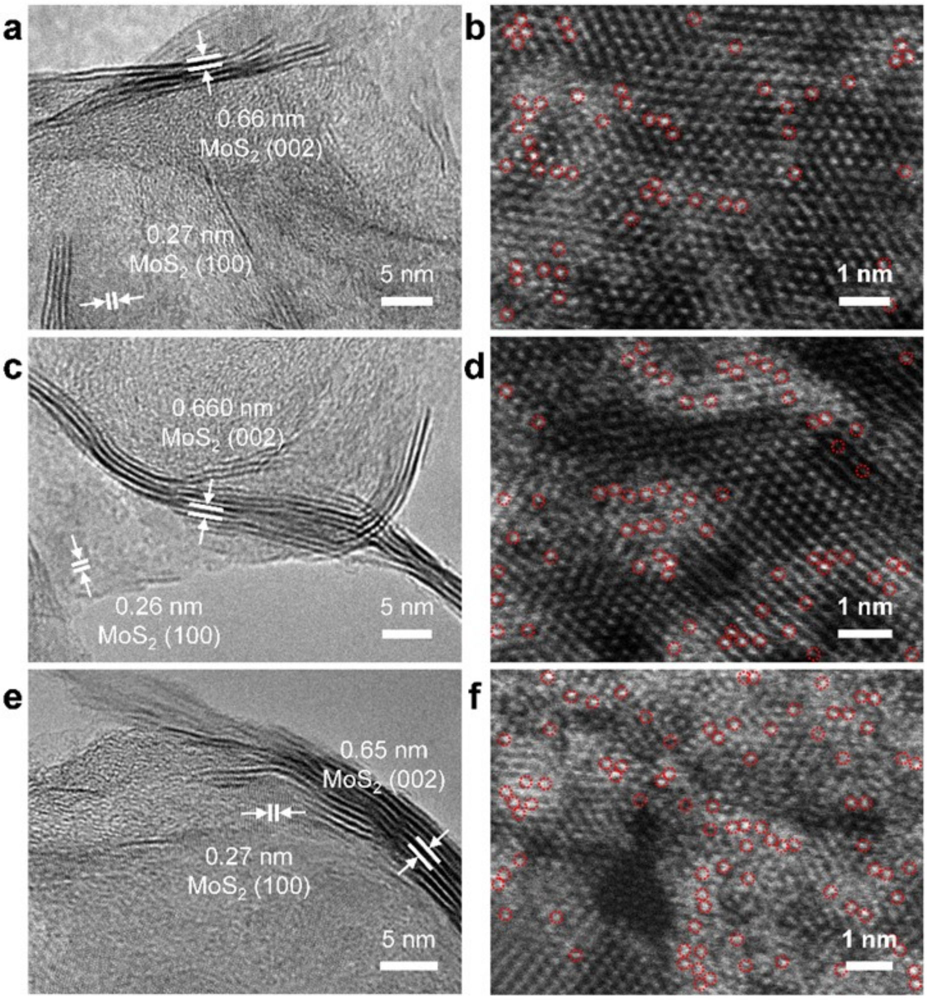

Figure S13. TEM images of (a) MoS$_2$/C-SAV, (c) MoS$_2$/C-SAFe, and (e) MoS$_2$/C-SANi. AC-TEM images of (b) MoS$_2$/C-SAV, (d) MoS$_2$/C-SAFe, and (f) MoS$_2$/C-SANi.

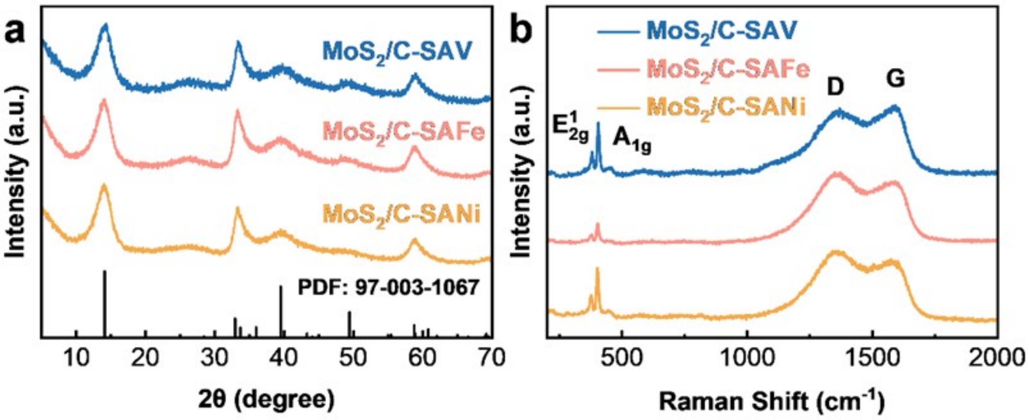

Figure S14. (a) XRD and (b) Raman of MoS_2/C-SAV, MoS_2/C-SAFe, and MoS_2/C-SANi.

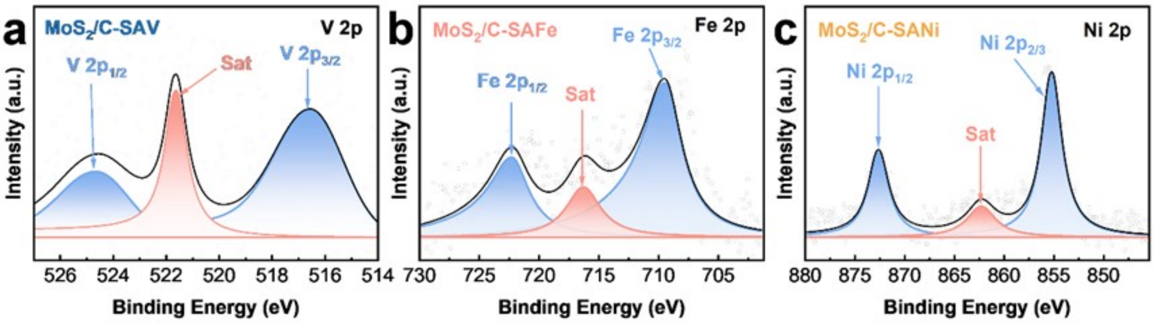

Figure S15. High-resolution XPS spectra of (a) V for MoS_2/C-SAV, (b) Fe for MoS_2/C-SAFe, and (c) Ni for MoS_2/C-SANi.

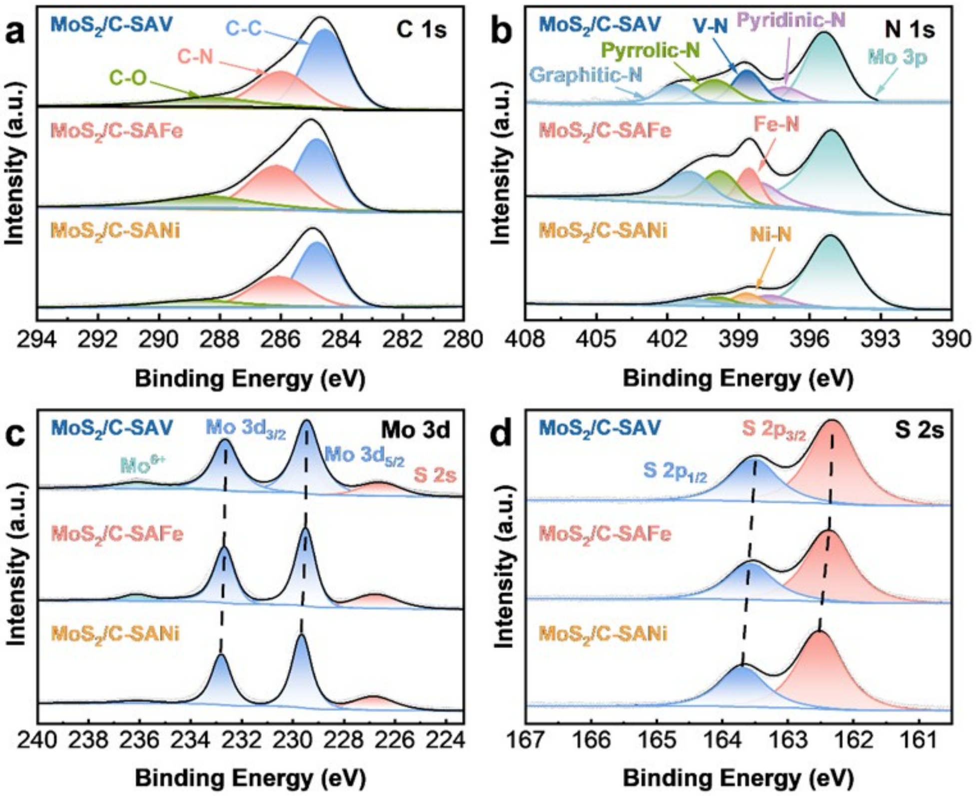

Figure S16. High-resolution XPS spectra of (a) C, (b) N, (c) Mo, and (d) S for MoS_2/C-SAV, MoS_2/C-SAFe, and MoS_2/C-SANi.

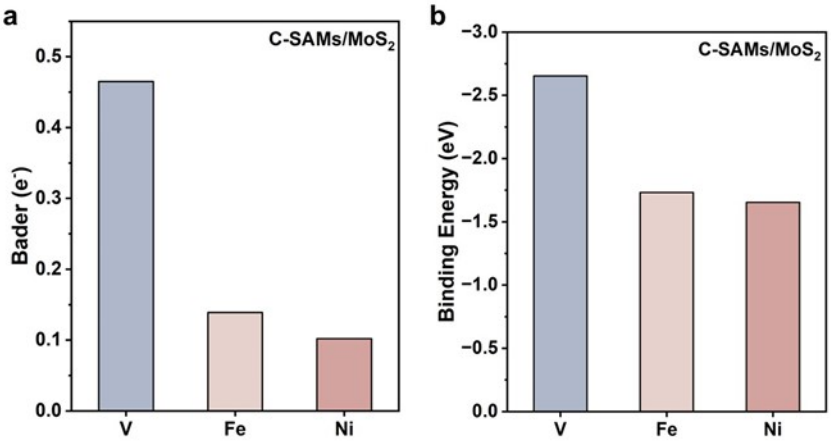

Figure S17. The (a) charge transfer and (b) binding energy between C-SAV, C-SAFe, C-SANi and MoS_2.

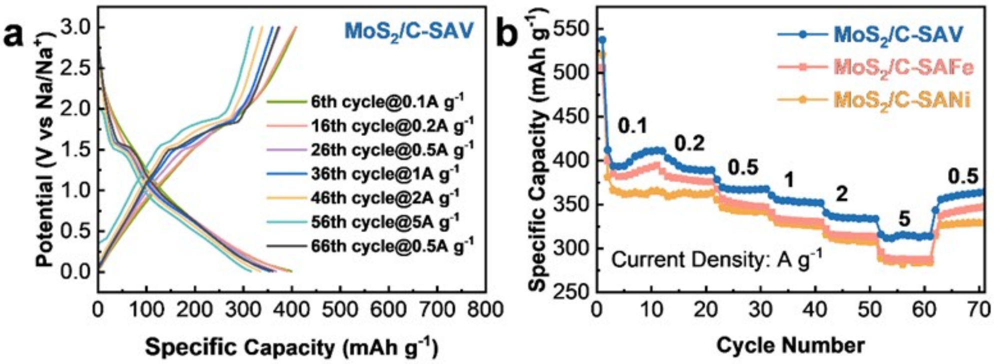

Figure S18. (a) GDC profiles of MoS_2/C-SAV. (b) Rate performance of MoS_2/C-SAV, MoS_2/C-SAFe, and MoS_2/C-SANi.

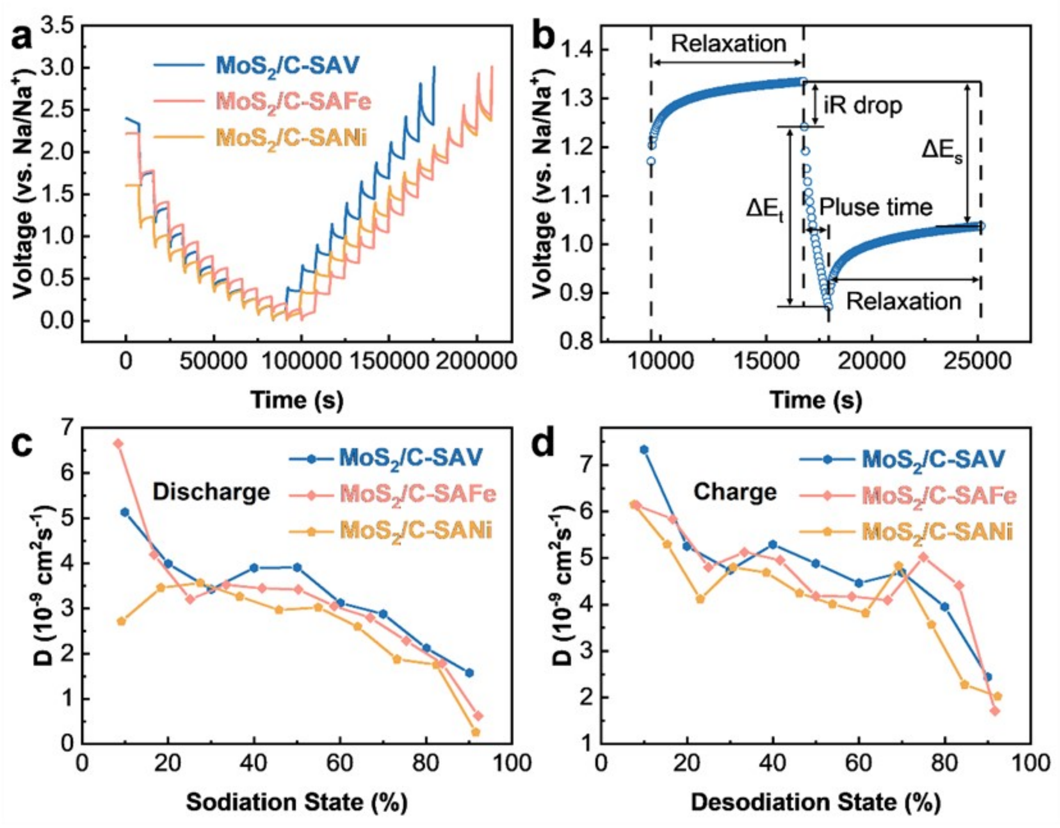

Figure S19. (a) GITT profiles of MoS$_2$/C-SAV, MoS$_2$/C-SAFe, and MoS$_2$/C-SANi. (b) Voltage *vs*. time profiles for a single GITT of MoS$_2$/C-SAV during the discharging process. Na$^+$ diffusion coefficients of MoS$_2$/C-SAV, MoS$_2$/C-SAFe, and MoS$_2$/C-SANi in the (c) discharging and (d) charging processes.

Table S1. The d band center (eV) of the metal atoms and the p band center (eV) of the N atoms in the C-SAMs substrate and in the frozen slab after S-atom adsorption on C-SAMs.

	C-SAMs		C-SAMs-S* frozen slab	
	d band center (M)	p band center (N)	d band center (M)	p band center (N)
C-SASc	-6.267	-7.127	-4.664	-7.476
C-SATi	-5.400	-7.050	-4.444	-7.446
C-SAV	-5.329	-7.107	-4.668	-7.325
C-SACr	-5.763	-7.195	-5.178	-7.181
C-SAMn	-3.543	-7.322	-3.870	-7.473
C-SAFe	-2.535	-7.195	-2.329	-7.299
C-SACo	-1.659	-7.003	-1.843	-7.149
C-SANi	-2.804	-7.364	-2.654	-7.428
C-SACu	-3.772	-7.208	-1.953	-6.530

Table S2. The adsorption energies (E_{ads}, eV) of Na, S and Na_2S on C-SAMs.

E_{ads}	Na	S	Na_2S
C-SASc	-0.742	-2.048	-4.871
C-SATi	-0.160	-3.057	-4.436
C-SAV	0.176	-2.506	-3.701
C-SACr	0.695	-0.693	-2.348
C-SAMn	0.378	-0.119	-1.721
C-SAFe	0.094	-0.102	-1.624
C-SACo	-0.314	0.683	-1.770
C-SANi	0.644	2.037	-0.816
C-SACu	0.726	1.877	-1.211

Table S3. The frozen slab adsorption energies (E_{fro}, eV) of Na, S and Na_2S on C-SAMs.

E_{fro}	Na	S	Na_2S
C-SASc	0.356	-1.138	-3.843
C-SATi	0.175	-2.817	-4.090
C-SAV	0.266	-2.565	-3.671
C-SACr	0.679	-0.955	-2.616
C-SAMn	0.359	-0.541	-2.166
C-SAFe	0.065	-0.407	-1.727
C-SACo	-0.330	0.429	-1.950
C-SANi	0.630	1.757	-0.907
C-SACu	0.710	0.572	-2.116

Table S4. The Integrated Crystal orbital Hamilton population (ICOHP) values of the M-S bonds when C-SAMs adsorbs S.

	ICOHP(M-S)
C-SASc	-1.582
C-SATi	-2.038
C-SAV	-2.006
C-SACr	-2.704
C-SAMn	-2.262
C-SAFe	-2.047
C-SACo	-1.436
C-SANi	-0.845
C-SACu	-2.165

Table S5. The ICOHP values of the Na-S bonds in Na_2S when C-SAMs adsorbs Na_2S.

	ICOHP(Na-S)
C-SASc	-0.519
C-SATi	-0.497
C-SAV	-0.515
C-SACr	-0.461
C-SAMn	-0.525
C-SAFe	-0.545
C-SACo	-0.527
C-SANi	-0.559
C-SACu	-0.425

Table S6. The features used in the SISSO computation.

	Units	Description
Ra	pm	Atomic radius of the metal atom
Rc	pm	Covalent radius of the metal atom
Rm	pm	Metallic radius of the metal atom
E_{fir}	KJ/mol	The first ionization energy of the metal atom
E_{sec}	KJ/mol	The second ionization energy of the metal atom
E_{af}	KJ/mol	The proton affinity of the metal atom
W_m	g/mol	The molar mass of the metal atom
V_m	cm^3/mol	The volume of the metal atom
WF_m	eV	The work function of the metal atom
Mag_m	μB	The magnetic moment of the ground state of the metal atom
χP		Pauling electronegativity of the metal atom

Table S7. Mathematical operators employed in SISSO calculation.

Mathematical operators	Description
+	Addition
-	Subtraction
*	Multiplication
/	Division
exp	Exponential function
exp-	Negative exponential function
^-1	Negative first power
^2	Square power
^3	Cube power
sqrt	Square root
log	Logarithms
|-|	Absolute value

Table S8. SISSO descriptor formula and its corresponding coefficients.

	$E = k_1\left({}^{R_m}/R_c\right) + k_0$	
Task	k_1	k_0
$E_{bar}(Na_2S)$	5.559	-3.504

Table S9. Prediction errors (eV) of $E_{bar}(Na_2S)$ using SISSO descriptor.

$E_{bar}(Na_2S)$	Prediction Error
C-SASc	0.019
C-SATi	-0.048
C-SAV	0.061
C-SACr	-0.135
C-SAMn	0.057
C-SAFe	-0.079
C-SACo	-0.119
C-SANi	0.104
C-SACu	0.141

Table S10. Comparison of rate performance of MoS_2/C-SAV with MoS_2-based anode materials for SIBs reported previously[7-13].

Materials	Current density (A g^{-1})	Capacity (mAh g^{-1})	Ref
MoS_2/C-SAV	0.1, 0.2, 0.5, 1, 2, 5	398.8, 391.0, 366.8, 353.7, 334.8, 315.7	This work
P-MoS_2@C/CNTP	0.1, 0.5, 1, 2, 5	375.6, 329.4, 297.8, 218.8, 149.5	7
Cu_2S@carbon@MoS_2	0.05, 0.1, 0.2, 0.3, 0.5, 1.0, 2.0, 3.0	430, 410, 386, 368, 359, 337, 316, 297	8
NPC@MoS_2/MXene	0.1, 0.2, 0.5, 1, 2, 5	428, 393, 346, 316, 289, 239	9
MoS_2@C-CMC	0.04, 0.08, 0.32, 0.64, 1	348, 321, 271, 230, 205	10
MS/C-H	0.2, 0.5, 1, 2, 5	227, 200, 196, 177, 148	11
MXene-MoS_2	0.1, 0.2, 0.5, 1, 2, 5	337, 321, 293, 266, 237, 190	12
MoS_2 NSs@TiO_2 NFs	0.5, 1, 2, 4	382.9, 342.0, 313.2, 254.2	13

Table S11. Comparison of long-life cycling performance of MoS_2/C-SAV with MoS_2-based anode materials for SIBs reported previously[7, 11, 14-19].

Materials	Current density (A g^{-1})	Capacity (mAh g^{-1})	Cycles	Decay rate per 100 cycles (%)	Capacity Retention (%)	Ref
MoS_2/C-SAV	5	332.8	1000	0.10%	98.87	This work
Co-MoS_2(1:8)/3DNC	1	292.0	1500	2.90%	56.50%	14
Fe-M-HoMS-Q	5	259.4	500	3.26%	83.68%	15
P-MoS_2@C/CNTP	1	252.9	1200	1.44%	82.73%	7
MS/C-H	2	158.0	1200	0.85%	89.77%	11
VO-MoS_2/N-RGO	1	245.0	1300	0.41%	94.65%	16
(MoS_2/CF)@MoS_2@C	1	332.6	1000	4.43%	55.71%	17
CoP-C@MoS_2/C	1	279.0	1000	0.98%	90.16%	18
TiO_2-MoS_2@NC-800	2	155.2	500	12.82%	35.91%	19

References

1. J. Hafner, Ab-initio Simulations of Materials using VASP: Density-Functional Theory and Beyond, *J. Comput. Chem.*, 2008, **29**, 2044-2078.
2. J. Moellmann and S. Grimme, DFT-D3 Study of Some Molecular Crystals, *J. Phys. Chem. C*, 2014, **118**, 7615-7621.
3. P. Wisesa, K. A. McGill and T. Mueller, Efficient Generation of Generalized Monkhorst-Pack Grids through the Use of Informatics, *Phys. Rev. B*, 2016, **93**, 155109.
4. G. Henkelman, B. P. Uberuaga and H. Jónsson, A Climbing Image Nudged Elastic Band Method for Finding Saddle Points and Minimum Energy Paths, *J. Chem. Phys.*, 2000, **113**, 9901-9904.
5. Y. Jiao, H. Li, Y. Jiao and S. Qiao, Activity and Selectivity Roadmap for C-N Electro-Coupling on MXenes, *J. Am. Chem. Soc.*, 2023, **145**, 15572-15580.
6. S. Zhu, J. Li, C. He, N. Zhao, E. Liu, C. Shi and M. Zhang, Soluble Salt Self-Assembly-Assisted Synthesis of Three-Dimensional Hierarchical Porous Carbon Networks for Supercapacitors, *J. Mater. Chem. A*, 2015, **3**, 22266-22273.
7. S. Sui, H. Xie, M. Liang, B. Chen, C. Liu, E. Liu, B. Chen, L. Ma, J. Sha and N. Zhao, “Three-in-One” Multi-Level Design of MoS_2-Based Anodes for Enhanced Sodium Storage: from Atomic to Macroscopic Level, *Adv. Funct. Mater.*, 2022, **32**, 2110853.
8. Y. Fang, D. Luan, Y. Chen, S. Gao and X. W. Lou, Rationally Designed Three-Layered Cu_2S@Carbon@MoS_2 Hierarchical Nanoboxes for Efficient Sodium Storage, *Angew. Chem. Int. Ed.*, 2020, **59**, 7178-7183.
9. H. Pan, Y. Huang, X. Cen, M. Zhang, J. Hou, C. Wu, Y. Dou, B. Sun, Y. Wang, B. Zhang and L. Zhang, Hollow Carbon and MXene Dual-Reinforced MoS_2 with Enlarged Interlayers for High-Rate and High-Capacity Sodium Storage Systems, *Adv. Sci.*, 2024, **11**, 2400364.
10. X. Xie, T. Makaryan, M. Zhao, K. L. Van Aken, Y. Gogotsi and G. Wang, MoS_2 Nanosheets Vertically Aligned on Carbon Paper: A Freestanding Electrode for Highly Reversible Sodium-Ion Batteries, *Adv. Energy Mater.*, 2016, **6**, 1502161.
11. Y.-L. Ding, P. Kopold, K. Hahn, P. A. van Aken, J. Maier and Y. Yu, A Lamellar Hybrid Assembled from Metal Disulfide Nanowall Arrays Anchored on a Carbon Layer: In Situ Hybridization and Improved Sodium Storage, *Adv. Mater.*, 2016, **28**, 7774-7782.
12. T. Wang, K. Yao, Y. Hua, E. G. Shankar, R. Shanthappa and J. S. Yu, Rational Design of MXene-MoS_2 Heterostructure with Rapid Ion Transport Rate as an Advanced Anode for Sodium-Ion Batteries, *Chem. Eng. J.*, 2023, **457**, 141363.
13. K. Zhu, S. Gao, T. Bai, H. Li, X. Zhang, Y. Mu, W. Guo, Z. Cui, N. Wang and Y. Zhao, Heterogeneous MoS_2 Nanosheets on Porous TiO_2 Nanofibers toward Fast and Reversible Sodium-Ion Storage, *Small*, 2024, **20**, 2402774.
14. H. Xie, B. Chen, C. Liu, G. Wu, S. Sui, E. Liu, G. Zhou, C. He, W. Hu and N. Zhao, Engineering the Interfacial Doping of 2D Heterostructures with Good Bidirectional Reaction Kinetics for Durably Reversible Sodium-Ion Batteries, *Energy Storage Mater.*, 2023, **60**, 102830.
15. H. Zhang, S. Zhang, B. Guo, L.-j. Yu, L. Ma, B. Hou, H. Liu, S. Zhang, J. Wang, J. Song, Y. Tang and X. Zhao, MoS_2 Hollow Multishelled Nanospheres Doped Fe Single Atoms Capable of Fast Phase Transformation for Fast-charging Na-ion Batteries, *Angew. Chem. Int. Ed.*, 2024, **63**, e202400285.
16. P. Li, J. Y. Jeong, B. Jin, K. Zhang and J. H. Park, Vertically Oriented MoS_2 with Spatially Controlled Geometry on Nitrogenous Graphene Sheets for High-Performance Sodium-Ion Batteries, *Adv. Energy*

Mater., 2018, **8**, 1703300.

17. C. Cui, Z. Wei, J. Xu, Y. Zhang, S. Liu, H. Liu, M. Mao, S. Wang, J. Ma and S. Dou, Three-Dimensional Carbon Frameworks Enabling MoS_2 as Anode for Dual Ion Batteries with Superior Sodium Storage Properties, *Energy Storage Mater.*, 2018, **15**, 22-30.
18. Y. Xia, T. Yang, Z. Wang, T. Mao, Z. Hong, J. Han, D.-L. Peng and G. Yue, Van der Waals Forces between S and P Ions at the CoP-C@MoS_2/C Heterointerface with Enhanced Lithium/Sodium Storage, *Adv. Funct. Mater.*, 2023, **33**, 2302830.
19. Y. Li, H. Wang, L. Wang, R. Wang, B. He, Y. Gong and X. Hu, Ultrafast Na^+-Storage in TiO_2-Coated MoS_2@N-Doped Carbon for High-Energy Sodium-Ion Hybrid Capacitors, *Energy Storage Mater.*, 2019, **23**, 95-104.